Lithuanian Journal of Physics
Vol. **64**, No. 4, pp. 259–275 (2024)
ISSN 1648-8504 eISSN 2424-3647
DOI: https://doi.org/10.3952/physics.2024.64.4.7

SINGLE-PIXEL RECONSTRUCTION IMAGING: TAKING CONFOCAL IMAGING TO THE EXTREME

S. Streckaite [a, b], D. Frolov [a], J. Chmeliov [b, c], A. Gelzinis [b, c], C. Ilioaia [a], S. Rimsky [d], R. van Grondelle [e], L. Valkunas [b], A. Gall [a], and B. Robert [a]

[a] *Université Paris-Saclay, CEA, CNRS, Institute for Integrative Biology of the Cell (I2BC), 91198 Gif-sur-Yvette, France*
[b] *Department of Molecular Compound Physics, Center for Physical Sciences and Technology, Saulėtekio 3, 10257 Vilnius, Lithuania*
[c] *Institute of Chemical Physics, Faculty of Physics, Vilnius University, Saulėtekio 9, 10222 Vilnius, Lithuania*
[d] *CIRB, Collège de France, Université PSL, CNRS, INSERM, 75005 Paris, France*
[e] *Department of Physics and Astronomy, Vrije Universiteit Amsterdam, De Boelelaan 1081, 1081HV Amsterdam, The Netherlands*
Email: bruno.robert@I2bc.paris-saclay.fr

Received 3 July 2024; accepted 29 July 2024

Light nanoscopy is attracting widespread interest for the visualization of fluorescent structures at the nanometre scale. Recently, a variety of methods have overcome the diffraction limit, yet in practice they are often constrained by the requirement of special fluorophores, nontrivial data processing, or a high price and complex implementation. Therefore, confocal microscopy, yielding a relatively low resolution, is still the dominant method in biosciences. It was shown that image scanning microscopy (ISM) with an array detector could improve the resolution of confocal microscopy. Here, we review the principles of the confocal microscopy and present a simple method based on ISM with a different image reconstruction approach, which can be easily implemented in any camera-based laser-scanning set-up to experimentally obtain the theoretical resolution limit of confocal microscopy. Our method, single pixel reconstruction imaging (SPiRI), enables high-resolution 3D imaging utilizing image formation only from a single pixel of each of the recorded frames. We achieve the experimental axial resolution of 330 nm, which was not shown before by basic confocal or ISM-based systems. The SPiRI method exhibits a low lateral-to-axial FWHM aspect ratio, which means a considerable improvement in 3D fluorescence imaging. As a demonstration of SPiRI, we present the 3D-structure of a bacterial chromosome with an excellent precision.

Keywords: fluorescence imaging, microscopy, point-spread function, super-resolution, confocal microscopy, bacterial chromosome

1. Introduction

Super-resolution fluorescence microscopy, or nanoscopy, the discovery of which was awarded the Nobel Prize in Chemistry in 2014 [1], has already led to remarkable progress in cell biology [2–4]. It is attracting increasing attention for the nanometre-scale visualization of fluorescent structures, wherein the emerging improvements in this field encourage application of nanoscopy in life science research as well as in other fields such as synthetic (bio)material science [5, 6].

From a general point of view, achieving nanoscale resolution requires one to overcome the diffraction limit – a fundamental physical limitation, discovered by Abbe almost 150 years ago, which states that light cannot be focused by any optical system to a spot smaller than approximately half its wavelength [7]. Consequently, in conventional light microscopy, the lateral and axial values of full widths at half maximum (FWHM) of the point-spread function (PSF), which define the maximum resolution of the approach, are in the 200–400 and 500–800 nm ranges, respectively. These limits were

circumvented by making use of photo-physical effects, computational methods, or a combination of both [8, 9]. The earliest (and most successful in terms of resolution) approaches rely either on single-molecule localization microscopy (SMLM) [10, 11] or stimulated emission depletion (STED) [12] and exhibit a resolution of a few tens of nanometres. Unfortunately, these methods have intrinsic experimental constraints, which sometimes limit their applicability and/or decrease their resolving power. In the last decade, a series of approaches were designed, yielding a lower resolution but an easier implementation. Structured illumination microscopy (SIM), in which the sample is excited in a wide field through grid-like structures to modulate the emission of the molecules, yields the lateral resolution of about 100–130 nm [13]. Several numerical treatments of the microscopy signals have also proven successful in improving the resolution. Some examples are super-resolution radial fluctuations (SRRF) yielding about 70–150 nm lateral resolution, but being rather limited for volumetric imaging [14, 15], or super-resolution optical fluctuation imaging (SOFI), which is based on the higher-order statistical analysis of temporal fluctuations and offers fivefold resolution enhancement in 2D [16], which makes it suitable for imaging of fluorescent blinking molecules.

For routine measurements in a cellular biology laboratory, however, many aspects of the imaging system are important, besides its intrinsic resolution. These aspects include the possibility to image living systems under relevant physiological conditions in three dimensions and to use the excitation light of low enough intensity to avoid sample photobleaching. In addition, the simplicity of sample preparation, of an imaging procedure and of data analysis must be taken into account. Existing nanoscopy approaches are now often implemented in large imaging facilities, and are still seldom present in individual cellular biology laboratories. To become routine, ideal super-resolution imaging methodologies should be simple, inexpensive to implement, and compatible with the conventional epifluorescence and confocal microscopies, as the latter are still currently the most popular technique for fluorescence imaging.

In laser-scanning confocal microscopy, the diffraction-limited resolution can theoretically be improved by about 1.4 times using an infinitely small pinhole [17]. In practice, however, the pinhole size is maintained large enough to avoid signal losses and diffraction phenomena. Confocal microscopy with commonly used pinholes of several tens of micrometres displays a marginal resolution increase, and its main interest resides in the sectioning ability and contrast enhancement [8, 14, 18–20]. Increasing the resolution of confocal microscopy was proposed a few decades ago [21] by making use of a detector array to collect emission information. This approach, image scanning microscopy (ISM), was predicted to provide a twofold increase in resolution upon reassignment of the detector pixels [22, 23]. Experimentally, ISM was shown to yield about 200–270 nm lateral resolution [24, 25], which can be improved to 150 nm for Fourier-filtered images [24] and to 193 nm with adaptive pixel reassignment (APR-ISM) [26]. This relatively simple approach constitutes the basis of the popular Airyscan commercial systems [27], in which each element of the detector represents a small pinhole that is several times smaller than those used in confocal microscopy. Also, based on standard confocal microscopy, rescan confocal microscopy (RCM), with an optical (rescanning) unit that projects the image on a CCD camera, provides a similar resolution [28].

In this work, we review the principles of the confocal scanning microscopy and present an even simpler method to experimentally achieve the theoretical limit of the resolution of confocal microscopy by improving the ISM detection procedure. This technique, single pixel reconstruction imaging (SPiRI), can be implemented in standard camera-based laser-scanning fluorescence imaging systems and straightforwardly applied for high-resolution 3D imaging. Its resolution is predicted to be 30% higher than that of classical confocal microscopy in all three dimensions, a value which we experimentally demonstrate by obtaining the PSF of an in-house built SPiRI imaging system using small fluorescent beads. Its excellent lateral-to-axial resolution ratio, which, to our knowledge, was not experimentally shown before for traditional confocal or basic ISM imaging systems, is particularly effective for 3D imaging, and we illustrate this by providing a 3D reconstruction of an *Escherichia coli* (*E. coli*) chromosome, stained with a fluorescent nucleic acid intercalator. This approach, which is here applied only to fluorescence imaging, can

be directly transferred to any type of emission microscopy, opening the way for achieving similar increases in resolution when using these techniques.

2. Methods

Microscopy. A commercial inverted epifluorescence microscope (Ti-U, *Nikon*, Champigny-sur-Marne, France) equipped with an 100x CFI PLAN APO objective lenses (*Nikon*, Champigny-sur-Marne, France) was coupled to an iXon Ultra 978 EMCCD camera (*Andor*, Belfast, UK), via a 2x Optomask (*Cairns Research*, Faversham, UK). Type F immersion oil (*Olympus*, Japan) was used for the objective lens. The excitation wavelength was provided by a 488 nm LX OBIS laser (*Coherent*, Les Ulis, France) and the beam collimated with a spatial filter assembly (KT310, LA1986-A; *Thorlabs*, Maisons Laffitte, France). Fluorescence emission was collected through the aforementioned microscope system equipped with an excitation filter (FL488-10; *Thorlabs*, Maisons Laffitte, France), a dichroic mirror (ZT488rdc; *Chroma Technology*, Vermont, USA) and an emission filter (GFP525-39; *Thorlabs*, Maisons Laffitte, France). Samples, sealed between two coverslips, were mounted in an in-house built sample holder and attached to an XY-translation stage (P-733.2CD; *Physik Instrumente*, Aix en Provence, France). In-house computer scripts controlled a DAC communications interface (PCU-100; *Andor*, Belfast, UK) to coordinate laser emission, the XYZ-nanopositioning system (E-725.3CD, P-733.2CD, P-725.4CD; *Physik Instrumente*, Aix en Provence, France) and camera acquisition. Typical exposition times were 15 and 7 ms per point during the fluorescing bead and *E. coli* nucleoid measurements, respectively. Emission of these samples was collected within a 505–545 nm window.

Image processing. Recorded SPiRI images were analyzed by custom-written software and post-processed with open-source image analysis platforms, Fiji [29] and Icy [30]. Deconvolution was carried out with a plugin [31] implemented in Fiji by using the Richardson–Lucy algorithm with total-variation regularization [32, 33]. Each 2D plane was deconvolved by using the regularization parameter set to 10^6, and 10 iterations were performed during the algorithm run with the experimentally obtained PSF (see the text). Volumetric 3D reconstructions from deconvolved 2D planes were performed with a Volume Viewer (Kai Uwe Barthel, *Internationale Medieninformatik*, *HTW Berlin*, Berlin, Germany) plug-in implemented in Fiji.

Bead measurements. Solutions of yellow-green (505/515) fluorescent carboxylated microspheres (F-8795; *Fisher Scientific*, Illkirch, France) of different sizes were diluted 10^4-fold with ethanol. A 5 Ml drop of the solution was spread over a coverslip and allowed to dry, yielding a low-density bead monolayer on the coverslip.

Bacterial strain, growth conditions, nucleic acids staining procedure and sample preparation. Escherichia coli HupAB cells were grown in the Luria Broth (LB) medium overnight at 30°C and at 160 rpm from single-colony isolates before being diluted. After 24 h, the cultures were diluted 1000-fold and grown further until they reached the mid-exponential phase (OD_{600} = 0.4 to 0.5). 500 Ml of culture was centrifuged and the pellet resuspended in the phosphate buffer (PBS). This procedure was repeated two times. Cells were then fixed for 20 min with a 3% formaldhehyde solution and subsequently washed a few times with PBS. Staining of the nucleic acids was performed by incubating the fixed cells for 20 min (in dark, on ice) with the SYBR® Gold (*Fisher Scientific*, Illkirch, France) stain. Aliquots of 5 Ml were deposited on 1.5% agarose pads mounted on a 22 Mm circular microscope coverslip (Ref. 011620; *Paul Marienfeld*, Lauda-Königshofen, Germany) fixed to a 1 mm deep silicone O-ring. After a few minutes, the sample was sandwiched by the addition of the second coverslip.

3. Image formation in optical microscopy: recalling the basics

The first step from conventional wide-field microscopy towards breaking the diffraction limit was made with the introduction of scanning microscopy [34]. The precision of the currently achievable mechanical movement is on the nanometre level or even below. Thus, as long as one controls variations in space that occur, for example, due to the translational movement of the sample, these changes can be recorded optically and then converted into higher-resolution images. This idea is one of the cornerstones of the SPiRI technique presented in this work. Before discussing this newly proposed method, however, let us briefly recall

the basic principles of image formation in optical scanning microscopy.

3.1. Intensity distribution of the focused excitation beam

Spatial distribution of the excitation intensity in the sample around the focus of the optics is usually described using the Huygens–Fresnel principle, according to which the amplitude of the electric field at the point $(\vec{r}' = (x, y, z)$ can be expressed as

$$E(\vec{r}) \propto \int E(\vec{r}') \frac{e^{ik|\vec{r}-\vec{r}'|}}{|\vec{r}-\vec{r}'|} d^2r'. \quad (1)$$

Here the integral is taken over the incoming wavefront confined by the aperture and $E(\vec{r}')$ is the amplitude of the electric field of the light wave at the point $\vec{r}'$ of the aperture of the lens. If the sample is located in the medium with the refractive index n, the wavevector is $k = 2\pi n/\lambda_{exc}$, λ_{exc} being the wavelength of the excitation laser in vacuum.

The integration in Eq. (1) is significantly simplified when the angle ϑ, at which the aperture is seen from the focus (see Fig. 1(a)), is small and assuming the plane incoming wavefront, i.e. $E(\vec{r}')$, is constant in the plane of the aperture. If the focal length F is much larger than the distance between the point $\vec{r}'$ and the focus (i.e. $x, y, z \ll F$), the integral in Eq. (1) can be calculated analytically, and when the point $\vec{r}'$ elongs to the focal plane (a blue point in Fig. 1(a)),

$$E(x, y, z = 0) \propto \frac{J_1(kr\vartheta)}{kr\vartheta}. \quad (2)$$

Here $r = \sqrt{x^2 + y^2}$ and $J_1(\xi)$ is the first-order Bessel function of the first kind. This leads to a well-known expression of the distribution of the focused light intensity around the focal point:

$$I_{exc}(x, y, 0) = |E(x, y, 0)|^2 = I_0^{(exc)} \left[\frac{2J_1(q)}{q}\right]^2, \quad (3)$$

where $I_0^{(exc)}$ is the intensity at the focal point $x = y = z = 0$ and

$$q = \frac{2\pi \cdot \mathrm{NA}}{\lambda_{exc}}, \quad (4)$$

with $\mathrm{NA} = n \sin\vartheta$ denoting the numerical aperture of the focusing optics. This expression reasonably describes the intensity distribution in the focal plane even when angle ϑ is not very small (up to $\vartheta \approx 30°$). Note that the irradiance distribution of linearly polarized light in the focal plane is no longer radially symmetric. However, even in such a case, the resulting difference between the actual FWHM of the irradiance distribution in the x and y directions and the one obtained from Eq. (3) (for which $\mathrm{FWHM}_{x,y} = 0.5145\lambda_{exc}/\mathrm{NA}$) does not exceed 10% [35].

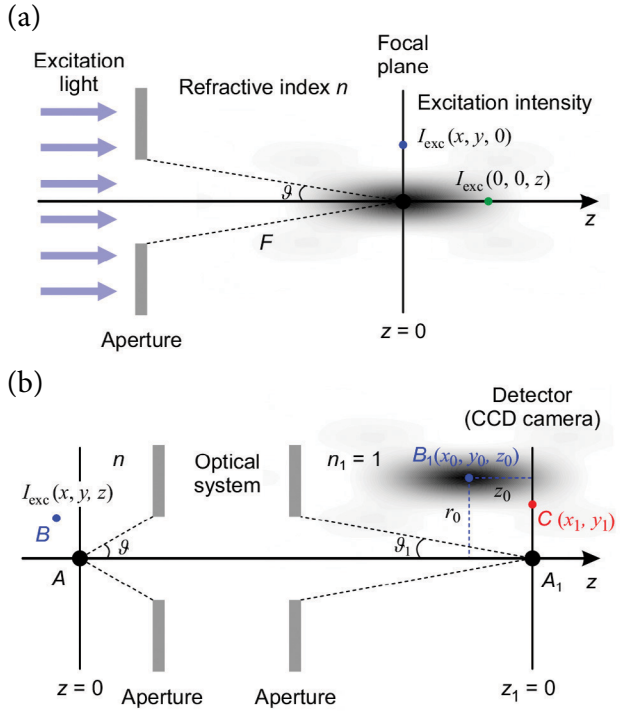

Fig. 1. (a) Intensity distribution of the focused excitation beam around the focus, see the text for details. (b) Registration of the fluorescence from a single emitter (point B) at the detector plane ($z_1 = 0$), see the text for details.

In the same limiting case (a small angle ϑ and a large F), a simple analytical expression of the irradiance distribution along the optical axis can also be obtained (a green point in Fig. 1(a)):

$$I_{exc}(0, 0, z) = I_0^{(exc)} \cdot \left[\frac{\sin w}{w}\right]^2, \quad (5)$$

where

$$w = \frac{\pi \cdot \mathrm{NA}}{\lambda_{exc}} \tan\left(\frac{\vartheta}{2}\right) z. \quad (6)$$

The FWHM of this distribution can be written as $\mathrm{FWHM}_z = 0.8859\lambda_{exc}/(\mathrm{NA} \cdot \tan(\vartheta/2))$, which is several times larger compared to the width of the radial distribution.

3.2. Intensity distribution of the focused emission signal

In the case of a single fluorophore randomly oriented at the point $\vec{r} = (x, y, z)$, the probability for this molecule to absorb a photon is proportional to the intensity of the excitation beam at this point, $W \propto I_{\text{exc}}(\vec{r})$. When this molecule is located precisely at the focus of this beam (point A in Fig. 1(b)), its emission is focused to the point A_1 on the other side of the optical system, thus producing a radial intensity distribution at the detector plane, similar to the one described by Eq. (3):

$$I_{\text{em}}(r_1, z_1 = 0) = I_0^{(\text{em})} \cdot \left[\frac{2J_1(q_1)}{q_1}\right]^2, \tag{7}$$

where

$$q_1 = \frac{2\pi \cdot \sin\vartheta_1}{\lambda_{\text{em}}} r_1. \tag{8}$$

The optical design of the microscope usually obeys the Abbe's sine condition $n \sin\vartheta = \sin\vartheta_1 \cdot M$, where M is the lateral magnification of the microscope. Thus q_1 can be rewritten in terms of the numerical aperture of the objective:

$$q_1 = \frac{2\pi \cdot \text{NA}}{\lambda_{\text{em}}} \frac{r_1}{M}. \tag{9}$$

When the molecule is shifted out of focus by a small (compared to the focal length) distance and is now located at the point B with coordinates (x, y, z), its fluorescence signal will produce a three-dimensional irradiance distribution $I_{\text{em}}(\vec{R})$ around the point B_1 with coordinates $x_0 = xM$, $y_0 = yM$ and $z_0 = zM^2/n$ with respect to the central point A_1. As a result, the detected fluorescence intensity at some point $C(x_1, y_1)$ in the detector plane $z_1 = 0$ will be equal to the products of $I_{\text{em}}(x_1 - x_0, y_1 - y_0, z_0)$ and the probability W of the molecule to be excited by the laser pulse, thus

$$I(x_1, y_1) \propto I_{\text{exc}}(x, y, z) \cdot I_{\text{em}}(x_1 - x_0, y_1 - y_0, z_0). \tag{10}$$

When the molecule remains in the focal plane of laser-focusing optics ($z = 0$), this expression can be simplified:

$$I(x_1, y_1) = I_0 \cdot \left[\frac{2J_1(q)}{q}\right]^2 \left[\frac{2J_1(q_1')}{q_1'}\right]^2, \tag{11}$$

with

$$q = \frac{2\pi \cdot \text{NA}}{\lambda_{\text{exc}}} \sqrt{x^2 + y^2} \tag{12}$$

and

$$q_1' = \frac{2\pi \cdot \text{NA}}{\lambda_{\text{em}}} \sqrt{\left(x - \frac{x_1}{M}\right)^2 + \left(y - \frac{y_1}{M}\right)^2}. \tag{13}$$

Alternatively, if the molecule remains on the optical axis, Eq. (10) simplifies to

$$I(x_1, y_1) = I_0 \left[\frac{\sin w}{w}\right]^2 \cdot I_{\text{em}}\left(x_1, y_1, z\frac{M^2}{n}\right), \tag{14}$$

where w is given in Eq. (6).

4. Single-pixel reconstruction imaging

4.1. xy plane

In confocal microscopy, as discussed above, the FWHM of the radial intensity distribution $I_{\text{exc}}(x, y)$ given in Eq. (3) is

$$\text{FWHM}_{x,y}^{(\text{exc})} \approx 0.5145 \frac{\lambda_{\text{exc}}}{\text{NA}}. \tag{15}$$

The light emitted by a single excited fluorophore focused on the CCD camera will display a similar intensity distribution $I_{\text{em}}(x, y)$. After rescaling the obtained image while taking into account the lateral magnification of the microscope, its FWHM will be

$$\text{FWHM}_{x,y}^{(\text{em})} \approx 0.5145 \frac{\lambda_{\text{em}}}{\text{NA}}, \tag{16}$$

where λ_{em} is the dominating emission wavelength. Usually, $\lambda_{\text{em}} > \lambda_{\text{exc}}$, therefore $I_{\text{em}}(x, y)$ is wider than $I_{\text{exc}}(x, y)$.

The amplitude of emission intensity distribution will be proportional to the probability of the molecule to be excited by the laser, which in turn depends on the excitation light intensity at that point (cf. colour profiles in the middle part of Fig. 2(a)). When a point fluorophore is moved within the focal plane, its fluorescence intensity will change according to the laser intensity at the position of the molecule, while its image will move on the detector array. If the size of the detector is small relative to the image of this point

fluorophore, the amplitude of the fluorescence recorded by this detector will change more than the amplitude of the excitation beam profile. Such a small detector can be a pixel of the CCD camera when the light intensity does not vary significantly over the entire pixel. The image of a region of interest (ROI) is constructed by using at each step the recorded intensity by this small detector. When a single emitter is located at some point with coordinates $(x, y, z = 0)$, let us analyze the intensity detected *just in the central pixel* of the CCD camera (the point A_1 in Fig. 1(b) and a shaded pixel in the middle part of Fig. 2(a)). If this pixel is small enough, by substituting $x_1 = y_1 = 0$ into Eq. 13) we obtain

$$I_{\text{image}}(x,y) = I_{\text{exc}}(x,y)\cdot I_{\text{em}}(x,y) = I_0 \cdot \left[\frac{2J_1(q)}{q}\right]^2 \left[\frac{2J_1(q_1')}{q_1'}\right]^2, \quad (17)$$

where $q_1' = q\lambda_{\text{exc}}/\lambda_{\text{em}}$ and q is given in Eq. (12). In other words, this method, which actually corresponds to confocal microscopy with a nano-sized detector, yields the absolute theoretical limit of confocal microscopy (corresponding to nanometre-sized pinholes). Being the product of two axially symmetric

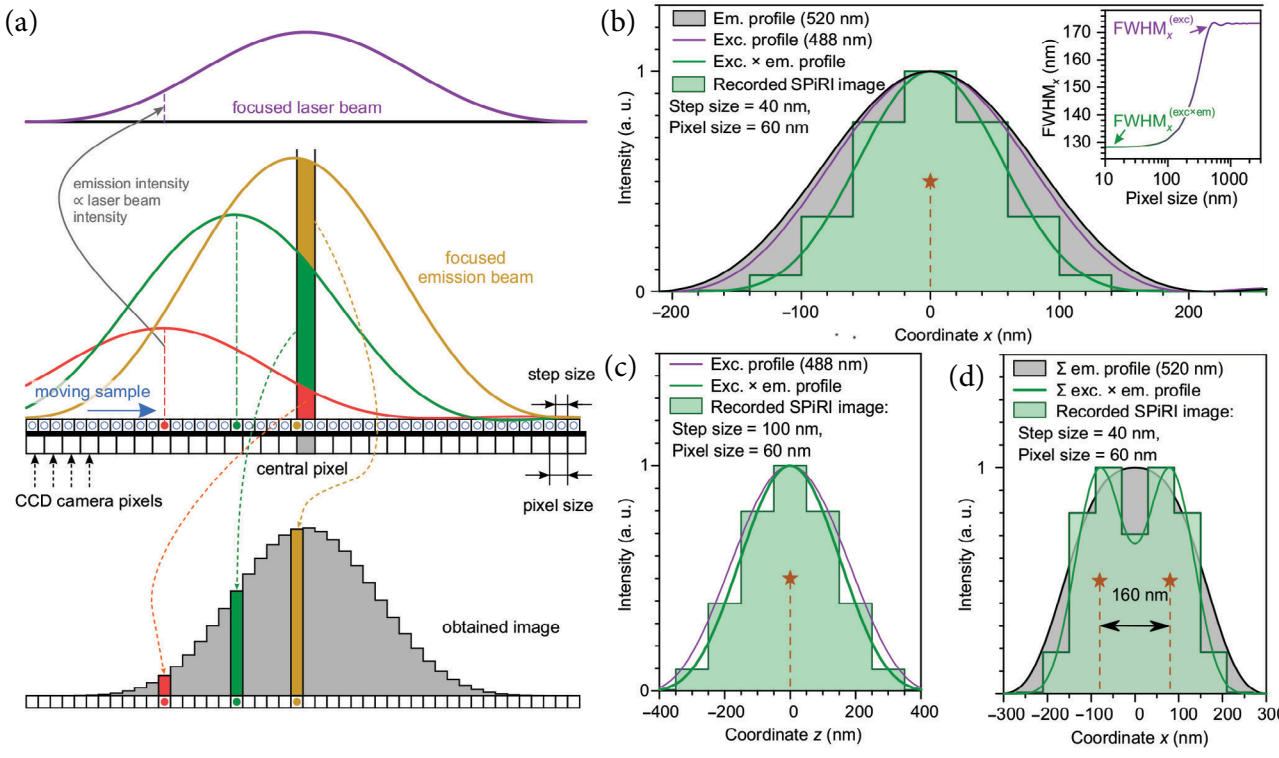

Fig. 2. Single pixel reconstruction imaging in a nutshell. (a) The principal scheme of the SPiRI data recording and image reconstruction for a one-dimensional (1D) case. The sample is scanned with a focused laser beam with a step size of tens of nanometres, and the final high-resolution image is reconstructed by assigning the value of the recorded intensity only from a single pixel (the one corresponding to the peak in the focused laser beam profile) of each of the recorded camera frames. The result of the scanning step size on the obtained reconstructed image is shown in Fig. 3. (b) Simulation of a single point emitter in 1D: the emission profile in conventional microscopy (a grey area), the intensity profile of the focused excitation laser beam (a purple line) and the reconstructed SPiRI image, obtained by using a scanning step of 40 nm (a green area). The SPiRI image corresponds to the discretized excitation × emission profile (a thick green line). The inset shows the dependence of the FWHM of the simulated image on the scanning pixel size. (c) Simulation of the axial distribution (z direction) of the SPiRI-recorded image of a single point emitter, obtained by scanning along the optical axis with a step size of 100 nm (a green area). (d) Simulation of the lateral fluorescence intensity distribution from two point emitters separated by 160 nm: the emission profile after laser excitation exhibits a single flat top (a grey area), while in the SPiRI-reconstructed image both emitters can be clearly distinguished, due to a significant (~32%) intensity drop between the two observed peaks. All the simulations were performed assuming $\lambda_{\text{exc}} = 488$ nm, $\lambda_{\text{em}} = 520$ nm and NA = 1.45, corresponding to our experimental conditions.

distributions, Eq. (17) defines a narrower distribution; its FWHM is determined by both the laser excitation wavelength and the dominating emission wavelength of the molecule:

$$\mathrm{FWHM}_{x,y}^{\mathrm{image}} \approx \left[(\mathrm{FWHM}_{x,y}^{\mathrm{exc}})^{-2} + (\mathrm{FWHM}_{x,y}^{\mathrm{em}})^{-2} \right]^{-1/2} \approx \frac{0.5145}{\mathrm{NA}} \left[\lambda_{\mathrm{exc}}^{-2} + \lambda_{\mathrm{em}}^{-2} \right]^{-1/2}. \quad (18)$$

The numerical simulations of the SPiRI method applied to a single point emitter are shown in Fig. 2(b). In conventional wide-field fluorescence microscopy, the registered distribution (Fig. 2(b), a gray shaded area) of $I_{\mathrm{em}}(x, y)$ would be mainly determined by the emission wavelength λ_{em} (for λ_{em} = 520 nm and NA = 1.45, $\mathrm{FWHM}_{x,y}$ = 185 nm). In confocal scanning microscopy (when the image is recorded by a photomultiplier), the distribution $I_{\mathrm{exc}}(x, y)$ will be somewhat narrower, determined by the laser excitation wavelength λ_{exc} (for λ_{exc} = 488 nm and the same NA = 1.45, $\mathrm{FWHM}_{x,y}$ = 173 nm). By contrast, SPiRI results in the discretized form of Eq. (17) that represents an even narrower distribution than either I_{exc} or I_{em}. The pixel size of the obtained image is equal to the step size of the scanning procedure, and for the conditions described above, $\mathrm{FWHM}_{x,y}$ = 126 nm. As shown in Fig. 2(d), such an approach can distinguish two point emitters separated by only 160 nm. The inset of Fig. 2(b) shows that using a larger detector leads to the situation corresponding to that of a large physical pinhole of confocal microscopy, which results in a significant drop in resolution.

4.2. z direction

Along the z axis, the axial FWHM can be determined analogically, by moving a single emitter along the optical axis. In such a case, from Eq. (14) we obtain:

$$I_{\mathrm{image}}(z) = I_0 \left[\frac{\sin w}{w} \right]^2 \left[\frac{\sin w_1}{w_1} \right]^2, \quad (19)$$

where

$$w_1 = \frac{\pi \cdot \sin \vartheta_1}{\lambda_{\mathrm{em}}} \tan\left(\frac{\vartheta_1}{2} \right) z_0 \overset{M \gg 1}{\approx} \frac{\pi \cdot \mathrm{NA}^2}{2\lambda_{\mathrm{em}} n} z. \quad (20)$$

The FWHM of this distribution is

$$\mathrm{FWHM}_z^{\mathrm{image}} \approx \frac{0.8859}{\mathrm{NA}^2} \left[\left(n + \sqrt{n^2 - \mathrm{NA}^2} \right)^{-2} \lambda_{\mathrm{exc}}^{-2} + (2n\lambda_{em})^{-2} \right]^{-\frac{1}{2}}. \quad (21)$$

The numerical simulations for the single emitter moving along the axial direction are shown in Fig. 2(c). For the same wavelengths as above and a sampling area of 60 × 60 nm on each CCD camera pixel, we obtain FWHM_z = 345 nm. In confocal scanning microscopy with an infinitely large pinhole, one would get 397 nm, see a purple line in Fig. 2(c).

To summarize, for λ_{em} = 520 nm, λ_{exc} = 488 nm and NA = 1.45, the application of SPiRI to a single point emitter theoretically results in $\mathrm{FWHM}_{x,y}$ = 126 nm and FWHM_z = 345 nm, while confocal microscopy results in significantly larger values of $\mathrm{FWHM}_{x,y}$ = 185 nm and FWHM_z = 398 nm.

In real measurements, the image obtained using a microscope objective is further enlarged. This allows one to choose the magnification factor of the optical system and the pixel size of the CCD detector in such a way that once projected on to a CCD camera, the registered image of a point fluorophore spreads over a minimum of three pixels in each detector dimensions. Then, one of these pixels (corresponding to the peak position of the focused laser beam) of the CCD camera can be used as the abovementioned effectively nano-sized detector required by SPiRI, although its actual size might be considerably larger.

4.3. Oversampling

Experimentally, the sample is moved across the focused laser beam with a predefined fixed step size, which determines the resolution of the final reconstructed image, i.e. the total number of pixels. Numerical simulations of the obtained images of a single and two closely located point emitters for excitation and emission wavelengths being λ_{exc} = 488 mm and λ_{em} = 520 nm, respectively (both intensity profiles are assumed to be expressed as Bessel functions given in Eq. (3)), with a CCD camera pixel size of 60 nm, and various step sizes used for sample movement are shown in Fig. 3. We

see that in all the cases, the obtained discrete intensity distributions follow the analytical product function of the excitation and emission profiles (Eq. (17)) in the case of a single emitter or the sum of two such functions, centred at their corresponding positions in the case of two point emitters (see red lines in Fig. 3). As expected, the latter continuous distribution might be seen as a limiting case of the registered discrete image when the step size → 0. Although reducing the step size (the so-called oversampling) does produce a smoother image, it does not reveal any additional details, hence during the actual measurement one should always choose between the image quality (its smoothness) and the total data acquisition time. Some image post-processing techniques (e.g. interpolation) may be used to mimic an oversampled image.

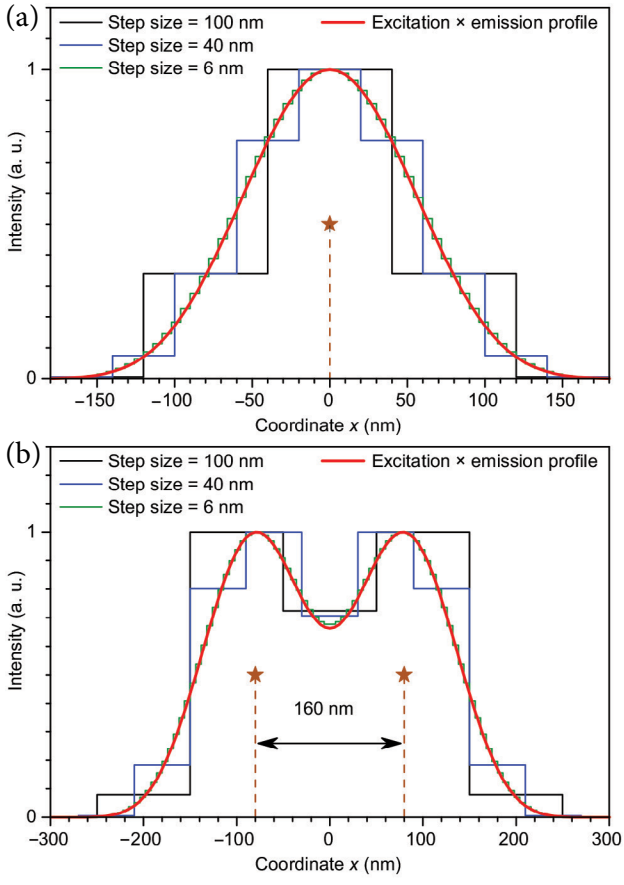

Fig. 3. Simulations of oversampling while performing scanning microscopy in the case of (a) a single emitter and (b) two point emitters separated by 160 nm. Simulations were performed using the same parameters as in Fig. 2(b, d): λ_{exc} = 488 mm, λ_{em} = 520 nm, NA = 1.45, pixel size = 60 nm. Step sizes are indicated in the legend.

5. Characterization of the point-spread function

5.1. Constructing the image of multiple emitters

The SPiRI method is not only extremely simple to implement, but it is also compatible with all image post-processing techniques utilized in confocal microscopy, such as deconvolution using the PSF [36]. Indeed, the numerical values for the FWHM of the registered image in the lateral and axial directions (shown in Fig. 2(b, c)) were obtained from simulating the signal of a single point emitter, and represent the theoretical limit for the resolution of SPiRI. In a more realistic case involving multiple emitters, it can be assumed (using a one-dimensional case for simplicity that is illustrated in Fig. 4) that the spatial excitation laser profile follows some function $P(x)$ (centred at its maximum position), and the emission profile of a single point emitter on the CCD camera plane is given by some other function $F(x)$ (again, centred at its maximum, i.e. the position of the emitter). The concentration of point emitters in the sample is given by some distribution function $S(x)$. Upon the movement of the sample across the laser excitation profile, for each position x_0 of the sample, the intensity at various coordinates x will be registered, and the intensity distribution function $I(x_0, x)$ will depend on both of these coordinates.

The emission from a point located at x' (with respect to the central position of the sample) creates a signal at some point x of the CCD camera that is proportional to the product of the laser excitation intensity $P(x_0 + x')$, the concentration of the molecules at that point within the sample $S(x')$ and the emission profile $F(x - x_0 - x')$. Therefore, the total intensity at x can be calculated by integrating over the whole sample:

$$I(x_0, x) = \int P(x_0 + x')F(x - x_0 - x')\, S(x')\, dx'. \quad (22)$$

This expression, although similar to the convolution of some point-spread function (PSF) with the source function $S(x')$, is not exactly of the mathematical form of convolution. However, at the central pixel of the CCD camera (where $x = 0$), it yields the usual definition of convolution,

$$I(x_0, 0) = \int P(x_0 + x')\, F(-x_0 - x')\, S(x')\, dx' =$$

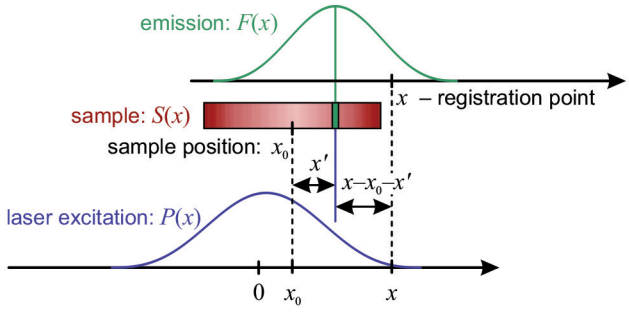

Fig. 4. Registration of the fluorescence from the one-dimensional extended light emitter. $P(x)$ denotes the laser excitation intensity profile in the focal plane of the objective, $F(x)$ shows the intensity distribution of a single point emitter as registered on the CCD camera, and $S(x)$ stands for the distribution of the point emitters within the sample. See the text for more details.

$$= \int \mathrm{PSF}\,(x_0 + x')\,S(x')\,\mathrm{d}x'$$

$$\equiv (\mathrm{PSF} * S)\,(x_0), \tag{23}$$

where we denoted $\mathrm{PSF}(x_0) = P(x_0)\,F(-x_0)$. For a symmetrical emission profile (i.e. if $F(-x) = F(x)$), we obtain the simple relation $\mathrm{PSF}(x_0) = P(x_0)\,F(x_0)$, which is just the 1D case of the more general expression in Eq. (17).

In the ideal case, the PSF could be determined as the product of the light intensity distributions of the focused excitation and emission signals. The analytical expression of these distributions in terms of the Bessel or sinc functions can be obtained only in the simplest cases discussed above, assuming mostly coaxial light propagation, ideal focusing, no aberrations, etc. The realistic PSF must be determined experimentally by obtaining the image of a point emitter – a small enough nm-sized fluorescent object. Simulations of the images of 'flat beads' of different sizes, performed for λ_{exc} = 488 nm and λ_{em} = 520 nm (see Fig. 5), revealed that all beads with a diameter smaller than 50 nm produced the same SPiRI images, and can thus be considered as a single point emitter.

5.2 Experimental measurements of the PSF

The experimental PSF of SPiRI was obtained by imaging 47-nm-sized fluorescing beads. Beads

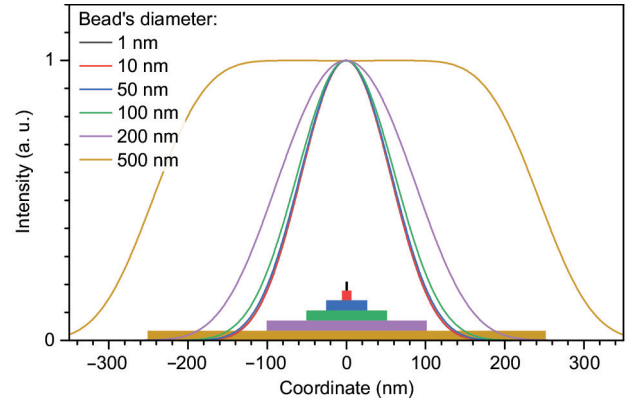

Fig. 5. Intensity distribution across the radial cross-section of the simulated SPiRI images that were obtained for the emitting circles of various diameters ('flat beads'). Simulations were performed using the same parameters as in Fig. 2(b): λ_{exc} = 488 mm, λ_{em} = 520 nm, NA = 1.45, pixel size = 60 nm. To obtain smooth distributions, a very small step size of 1 nm was used. Coloured bars on the x axis represent the size of the corresponding bead.

were scanned with 20-nm x and y steps, and 100-nm z steps, and the final image was reconstructed by using either the whole area detector (equivalent to confocal microscopy, see Fig. 6(a)) or only the central pixel (SPiRI, see Fig. 6(b)). A ~30% gain in the lateral and axial resolution (Fig. 6(c, d), respectively) is observed for SPiRI as compared to confocal microscopy, in agreement with the theoretical predictions. The lateral and axial cross-sections of the resulting 3D PSF (see Fig. 6(e)) are obtained using SPiRI (Fig. 8 in the Appendix), and the yield FWHM of 165, 182 and 329 nm in the x, y and z directions, respectively (see also Table 1 in the Appendix), shows that the method yields an extremely low axial/lateral FWHM aspect ratio, which on an average is around 1.7.

Validation of the PSF was achieved by convolving the Gaussian PSF (for simplicity, using $\mathrm{FWHM}_{x:y:z}$ = 180 : 180 : 330 nm) with the spheres of 100, 220 and 500 nm in diameter. The calculated intensity distributions in the lateral cross-section exhibit a very good agreement with the actual experimental results of differently-sized beads, see Fig. 6(f). An example of the deconvolution procedure using an experimentally obtained PSF, resulting in a recovery of an actual size of 100-nm bead, is shown in Fig. 9 in the Appendix.

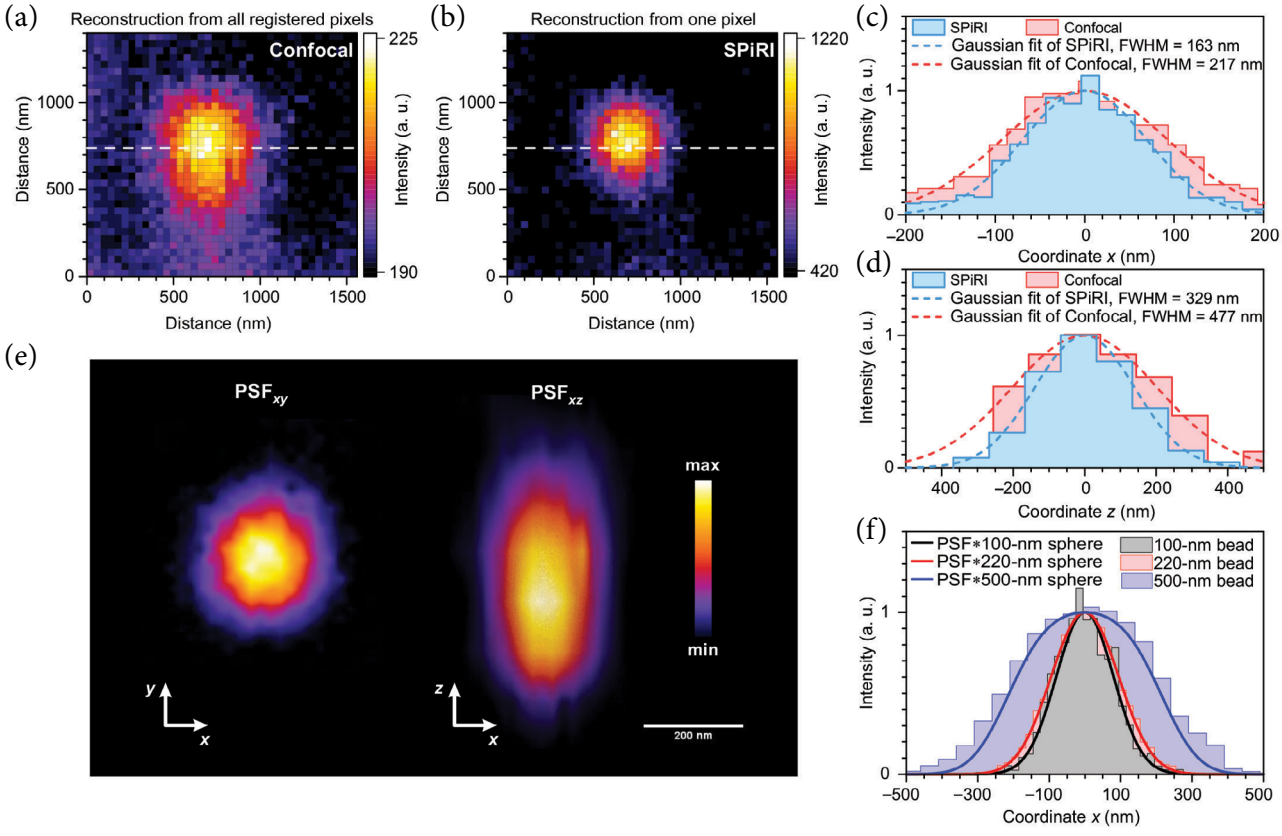

Fig. 6. Bead measurements using the SPiRI and determination of the experimental PSF. (a) Reconstructed image of a 47-nm bead, obtained by summing over the 30 × 30 pixel detector area (as in confocal microscopy). (b) Reconstructed image of a 47-nm bead, obtained by the SPiRI method. (c) Horizontal cross-sections of the reconstructed images in panels (a) and (b) along the white dashed line (red and blue shaded areas, respectively) and their respective Gaussian fits (dashed lines). (d) Axial distribution of the fluorescence intensity from the 47-nm bead, obtained by using SPiRI and confocal techniques (red and blue shaded areas, respectively) and their respective Gaussian fits (dashed lines). (e) Cross-sections in the *xy* and *xz* planes of the three-dimensional PSF of the SPiRI system, obtained from the reconstruction of the 47-nm bead images. (f) Lateral cross-sections of the SPiRI images of variously sized beads (shaded areas), compared to the numerical convolution of the three-dimensional Gaussian PSF ($FWHM_{x:y:z}$ = 180 : 180 : 330 nm) from the panel (e) with a three-dimensional sphere of a corresponding bead size (solid lines). The experimental cross-sections in lateral and axial directions (panels (c, d)) were fitted with the Gaussian functions, thus also obtaining the mean background intensity level. This background was subtracted and the resulting experimental distributions were rescaled so that their Gaussian fits were normalized to the 0–1 interval. For panels (a–d), a 47-nm bead was scanned by 20-nm *x* and *y* steps, and 100-nm *z* steps; 3D reconstruction of PSF obtained from 9 planes in the *z* direction. For panel (f), 100- and 200-nm beads were scanned by 20-nm *x* and *y* steps, and a 500-nm bead was scanned by 47-nm *x* and *y* steps.

6. Example of 3D imaging by SPiRI: *E. coli* nucleoid

SPiRI is in principle applicable to any type of an emitting sample. As an example of the application of the method, images were obtained for the *E. coli* nucleoid with SYBRö Gold, a cyanine-based fluorescent nucleic acid intercalator. Whole *E. coli* cells were scanned with 40-nm *x* and *y* steps, and 200-nm *z* steps using 488-nm laser excitation; the emission of SYBRö Gold was collected at the 505–545 nm region (see Fig. 7(a) and Fig. 10 in the Appendix). While confocal microscopy could barely distinguish details in this structure, the SPiRI images reveal many more details (see the intensity profiles in Fig. 7(b)). To enhance these structural features, each image along the *z* axis was deconvolved using the experimentally determined PSF (Fig. 7(a)).

The outstanding axial resolution of the SPiRI approach allowed us to construct a volumetric 3D

image of the *E. coli* nucleoid (see Fig. 7(c)). Several cross-sections of the reconstruction are shown in Fig. 7(d) (sectioning of the whole 3D reconstruction can be seen in Fig. 11 in the Appendix). The resulting nucleoid structure exhibits two longitudinal high-density regions as described previously, but its shape appears much clearer in the SPiRI images [37]. Substructures can be observed in each of the high-density regions (Fig. 7(c)), and cylindroids that constitute subdomains appear clearly. These SPiRI images reveal the 3D structure of the bacterial chromosome with an unprecedented precision. The highly structured architectures vary from cell to cell, depending on their growth phase stage. However, common features are maintained, such as elongation of the nucleoid throughout the cell, its cylindrical structure parallel to the cell wall [38–40], and its global twisting that was also documented before by BALM and PAINT methods [38, 39], although none of these methods allowed the 3D reconstruction of the whole nucleoid in the cell.

7. Concluding remarks

Several methodologies may nowadays provide theoretically diffraction-unlimited resolutions. Experimental constraints, however, often provide limitations to their resolving power, as well as to their general applicability (special requirement of fluorophores, insufficient photon budget, etc.) [9, 41]. Additional restrictions are induced by the use of non-trivial computational methods, which may lead to a risk of artefacts, or to difficulties in generating 3D structures [42, 43]. In the present state-of-the-art, a combination of different approaches is still necessary for achieving the most precise description of nanoscale structures [8, 44]. Such drawbacks complicate and hinder the application of fluorescence nanoscopy in biological and medical research, which is unfortunate as high-resolution fluorescence imaging has become an essential tool for characterizing nanostructures and their functions.

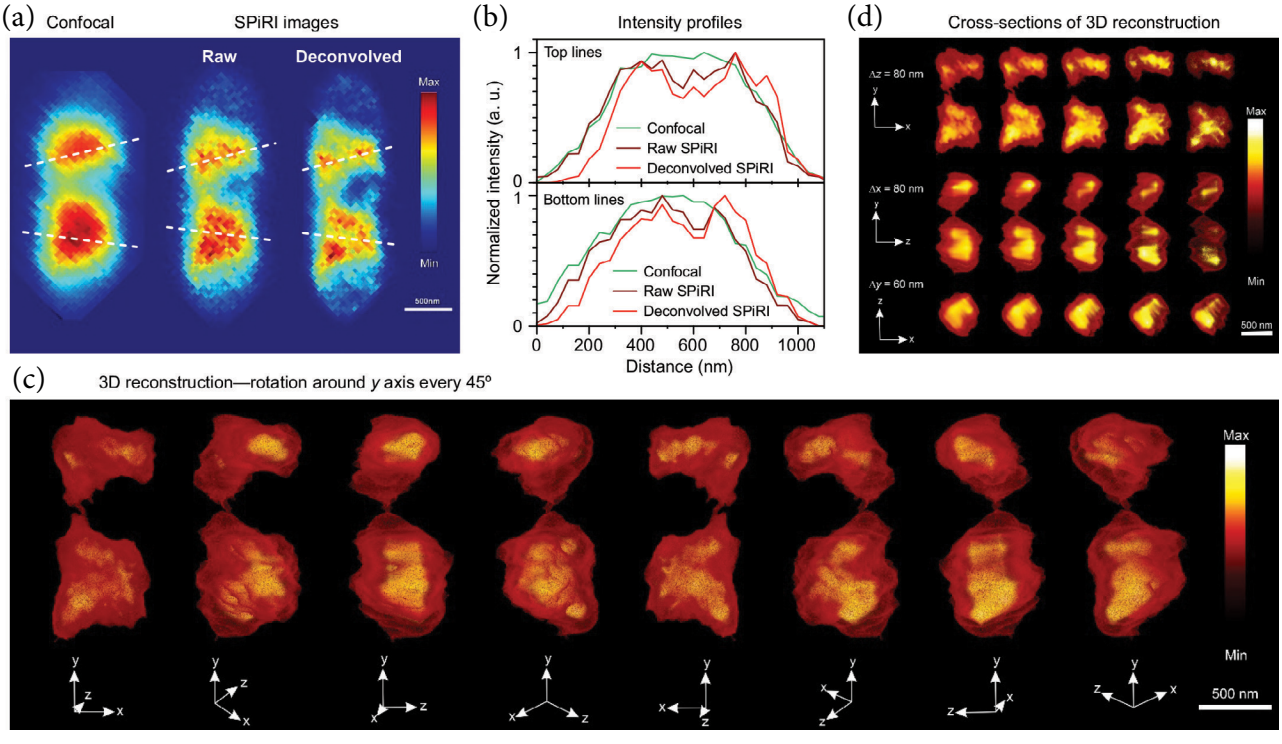

Fig. 7. *E. coli* nucleoid stained with SYBR® Gold. (a) Reconstructed confocal image and SPiRI images before and after deconvolution. (b) Intensity profiles along the white dashed lines in the panel (a) for a qualitative comparison of the resolution. Intensities of all images were normalized to the 0–1 interval. (c) 3D reconstruction from the deconvolved SPiRI images after scanning the whole cell. Each sequential image represents a clockwise rotation around the *y* axis by 45° with respect to the previous one. (d) Several cross-sections (by 60 or 80 nm steps) from the middle of the 3D reconstruction at the *x*, *y* and *z* orientations of the cell. The sample was scanned with 40-nm *x* and *y* steps, and 200-nm *z* steps, λ_{exc} = 488 nm, emission collected within a 505–545 nm window. 3D reconstruction was obtained from 12 planes.

The method described in this paper, SPiRI, adopts the advantages of ISM, yet avoids a sophisticated treatment of the recorded data, such as pixel reassignment (as in ISM), or higher-order statistical analysis (as in SOFI and its variants). In SPiRI, the intensity of only the central pixel of the camera is used for image construction. It results in a significant gain in resolution in all three dimensions, and a very good signal-to-noise ratio. It is worth noting at this stage that once the optical system is well-aligned and considering that about 3 pixels in each direction correspond to the FWHM of PSF, the number of photons reaching the central pixel is about 10% of the total photons emitted by the sample. The gain in resolution is thus achieved at the expense of a minimum signal loss.

Implementing SPiRI onto a classical fluorescence microscope, using 488 nm excitation and recording the green region, has allowed us to achieve a resolution of 180 and 330 nm in the lateral and axial directions, respectively, without any post-processing of the recorded data. Meticulous calibration of the optical system is predicted to further push the lateral resolution to its theoretical limit of 126 nm under the same excitation conditions. Furthermore, using any excitation and emission wavelength pair commonly used in biological and physical chemistry studies (Fig. 12), SPiRI is capable of providing lateral resolutions below 190 nm. This is the case even for the emission wavelengths that extend to the near-IR. As SPiRI methodology is fundamentally confocal fluorescence microscopy pushed to its limits (actually confocal fluorescence microscopy using a nano-sized detector), the generated images are compatible with any classical image post-processing techniques, like deconvolution using the experimentally measured PSF of the optical system. Improved resolution in all directions leads to a low lateral-to-axial resolution ratio and results in a considerable improvement for reconstructing precise 3D volumes. Other nanoscopy techniques exhibiting an excellent axial resolution exist; however, they are either complex to implement or limited in terms of depth [45, 46], while SPiRI can be implemented in common laser-scanning fluorescence imaging systems. From an experimental point of view, SPiRI is not more demanding than classical confocal microscopy, neither in terms of optics or laser excitation intensity, nor in terms of sample preparation, and can thus be applied to any class of fluorophore and to a wide range of samples of different sizes, fixed or living.

Finally, it must be noted that at higher resolution than 200 nm, optical microscopy characterization at the nanometre range is restricted to fluorescence, as existing super-resolution methods cannot be applied to other emission types. SPiRI being entirely grounded on a quite simple geometry of the signal acquisition and not generating large losses of signal intensity, may be used to generate Raman images at similar resolutions, just by introducing a modification of the emission wavelength selection. A SPiRI Raman microscope is being constructed on this basis, which will open the way for a high-resolution mapping of nanoscale structures containing precise chemical information.

Acknowledgements

This work was supported by the European Research Council (ERC) through an Advanced Investigator Grant, Contract No. 267333, PHOTPROT (C.I., A.Ga., B.R., D.F.); the French Infrastructure for Integrated Structural Biology (FRISBI) ANR-10-INBS-05-05 and the Infrastructures en Biologie Santé et Agronomie (IBiSA) (C.I., A.Ga., B.R, D.F.); the EU Horizon 2020 Research and Innovation Program under the Marie Skodowska-Curie, Agreement No. 675006 (S.S, A.Ga., C.I, B.R.); the European Union NextGenerationEU, Agreement No. 10-036-T-0009 (S.S.).

Appendix

Table 1. FWHM values (in nm) obtained by fits with a Gaussian function in lateral and axial planes of several 50-nm-diameter beads, scanned along x, y and z directions. Scanning step sizes: x and y directions 20 nm, z direction 100 nm. Excitation wavelength λ_{exc} = 488 nm, emission signal was collected from a 505–545 nm window. No background was removed from any of the images (background removal would result in slightly smaller FWHM values).

No.	Number of scanned z planes	SPiRI			Confocal		
		$FWHM_x$	$FWHM_y$	$FWHM_z$	$FWHM_x$	$FWHM_y$	$FWHM_z$
1	9	165	182	329	216	302	477
2	10	179	211	269	240	320	445
3	10	190	213	295	237	338	467
4	8	192	195	328	225	300	452
5	9	178	215	329	221	359	423
6	11	189	221	333	240	324	479
7	11	186	186	347	244	265	547
8	9	177	199	381	220	295	430
9	10	166	184	391	208	247	685
Average	10	180	200*	334	228	306*	489

* y axis is elongated with respect to the x axis due to the mechanical drift of x and y piezo stage.

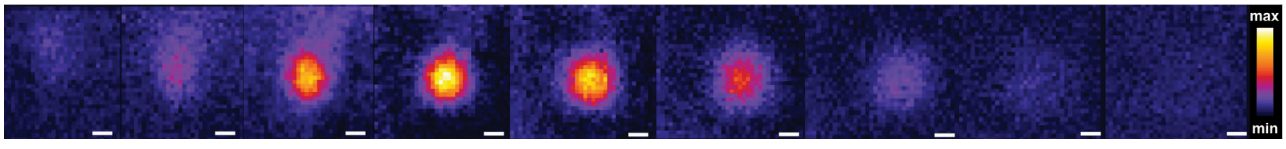

Fig. 8. z scans of a 50-nm bead. These images were input for the PSF shown in Fig. 6(e). Scanning step sizes: x and y directions 20 nm, z direction 100 nm. Excitation wavelength λ_{exc} = 488 nm, emission signal was collected from a 505–545 nm window. White bars correspond to 100 nm.

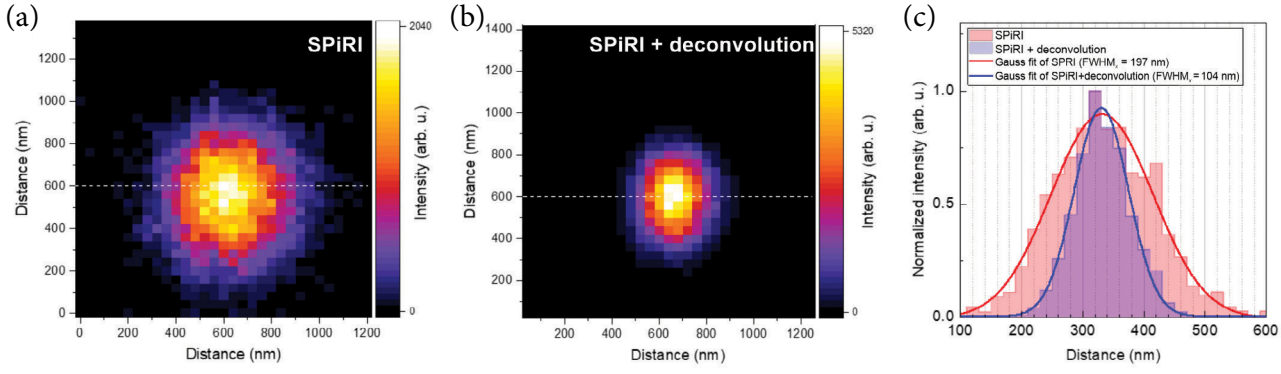

Fig. 9. 100-nm bead. (a) SPiRI image. (b) Deconvolved SPiRI image. PSF used for deconvolution was obtained experimentally from the 50-nm bead measurements: $FWHM_{xy}$ = 180 : 180 nm. (c) Comparison of $FWHM_x$ for SPiRI and deconvolved SPiRI images. The $FWHM_x$ after the deconvolution of the SPiRI image of 100-nm bead changes from 197 to 104 nm. Scanning steps for x and y directions 20 nm. Excitation wavelength λ_{exc} = 488 nm, emission was collected from a 505–545 nm window.

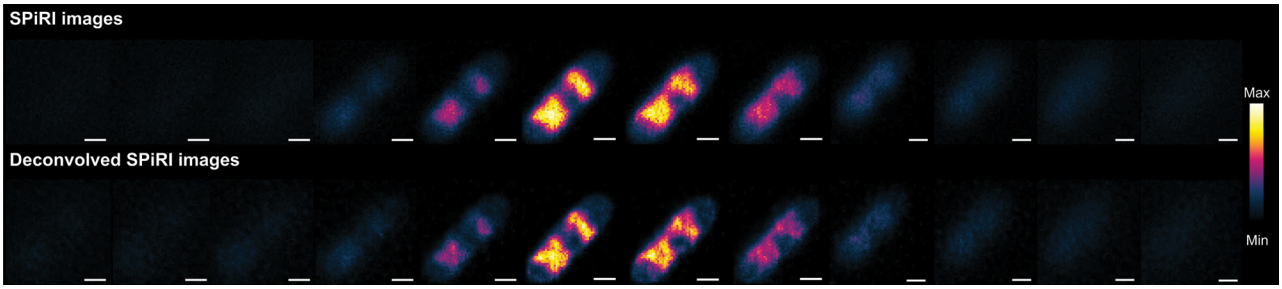

Fig. 10. *z* scans of an *E. coli* nucleoid labelled with SYBR® Gold. Top, SPiRI images. Bottom, deconvolved SPiRI images. PSF used for the deconvolution of each plane was obtained experimentally from the 50-nm bead measurements: FWHM_{xy} = 180 : 180 nm. Scanning step sizes: *x* and *y* directions 40 nm, *z* direction 200 nm. Excitation wavelength λ_{exc} = 488 nm, emission was collected from a 505–545 nm window. White bars correspond to 500 nm.

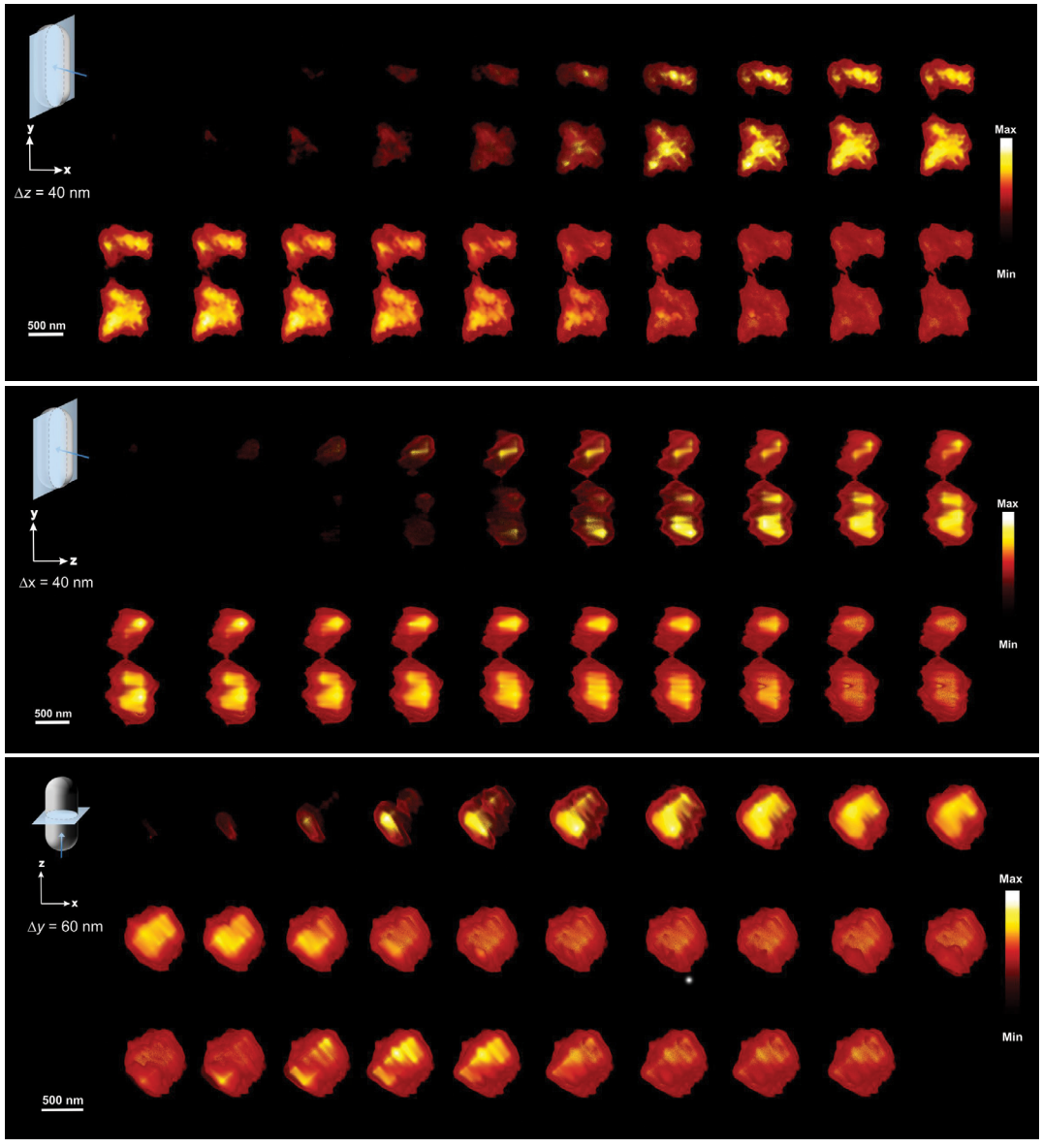

Fig. 11. *E. coli* nucleoid labelled with SYBR® Gold. Cross-sections (by 40 or 60 nm steps) of the 3D volumetric reconstruction at *x*, *y* and *z* orientations of the cell. The sample was scanned by 40 nm steps in *x* and *y* directions and 200 nm steps in the *z* direction. Excitation wavelength λ_{exc} = 488 nm, emission was collected from a 505–545 nm window. 3D reconstruction obtained from 12 planes.

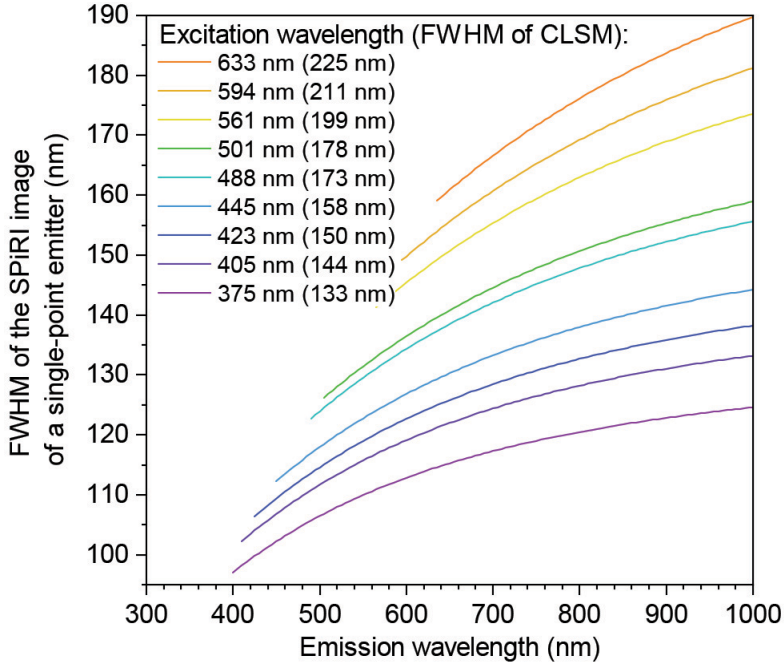

Fig. 12. Lateral resolution of SPiRI as a function of excitation and emission wavelengths. FWHM of confocal laser scanning microscopy (CLSM) is shown in the brackets next to the corresponding excitation wavelength as it is independent on the emission wavelength.

References

[1] L. Möckl, D.C. Lamb, and C. Bräuchle, Super-resolved fluorescence microscopy: Nobel Prize in Chemistry 2014 for Eric Betzig, Stefan Hell, and William E. Moerner, Angew. Chemie Int. Ed. **53**, 13972 (2014).

[2] S.J. Sahl, S.W. Hell, and S. Jakobs, Fluorescence nanoscopy in cell biology, Nat. Rev. Mol. Cell Biol. **18**, 685 (2017).

[3] Y.M. Sigal, R. Zhou, and X. Zhuang, Visualizing and discovering cellular structures with super-resolution microscopy, Science **361**, 880 (2018).

[4] M.S. Dietz and M. Heilemann, Optical super-resolution microscopy unravels the molecular composition of functional protein complexes, Nanoscale **11**, 17981 (2019).

[5] S. Pujals, N. Feiner-Gracia, P. Delcanale, I. Voets, and L. Albertazzi, Super-resolution microscopy as a powerful tool to study complex synthetic materials, Nat. Rev. Chem. **3**, 68 (2019).

[6] C.S. Hansel, M.N. Holme, S. Gopal, and M.M. Stevens, Advances in high-resolution microscopy for the study of intracellular interactions with biomaterials, Biomaterials **226**, 119406 (2020).

[7] E. Abbe, Beiträge zur theorie des mikroskops und der mikroskopischen wahrnehmung, Arch. für Mikroskopische Anat. **9**, 413 (1873).

[8] D. Li, L. Shao, B.-C. Chen, X. Zhang, M. Zhang, B. Moses, D.E. Milkie, J.R. Beach, J.A. Hammer, M. Pasham, et al., Extended-resolution structured illumination imaging of endocytic and cytoskeletal dynamics, Science **349**, aab3500 (2015).

[9] B. Vinçon, C. Geisler, and A. Egner, Pixel hopping enables fast STED nanoscopy at low light dose, Opt. Express **28**, 4516 (2020).

[10] E. Betzig, G.H. Patterson, R. Sougrat, O.W. Lindwasser, S. Olenych, J.S. Bonifacino, M.W. Davidson, J. Lippincott-Schwartz, and H.F. Hess, Imaging intra-cellular fluorescent proteins at nanometer resolution, Science **313**, 1642 (2006).

[11] M.J. Rust, M. Bates, and X. Zhuang, Sub-diffraction-limit imaging by stochastic optical reconstruction microscopy (STORM), Nat. Methods **3**, 793 (2006).

[12] S.W. Hell and J. Wichmann, Breaking the diffraction resolution limit by stimulated emission: Stimulated-emission-depletion fluorescence microscopy, Opt. Lett. **19**, 780 (1994).

[13] S. Hayashi, Resolution doubling using confocal microscopy via analogy with structured illumination microscopy, Jpn. J. Appl. Phys. **55**, 082501 (2016).

[14] S. Culley, K.L. Tosheva, P.M. Pereira, and R. Henriques, SRRF: Universal live-cell super-resolution microscopy, Int. J. Biochem. Cell Biol. **101**, 74 (2018).

[15] N. Gustafsson, S. Culley, G. Ashdown, D.M. Owen, P.M. Pereira, and R. Henriques, Fast live-cell conventional fluorophore nanoscopy with ImageJ through super-resolution radial fluctuations, Nat. Commun. **7**, 12471 (2016).

[16] T. Dertinger, R. Colyer, G. Iyer, S. Weiss, and J. Enderlein, Fast, background-free, 3D super-resolution optical fluctuation imaging (SOFI), Proc. Natl. Acad. Sci. USA **106**, 22287 (2009).

[17] T. Wilson, Resolution and optical sectioning in the confocal microscope, J. Microsc. **244**, 113 (2011).

[18] S.W. Hell, Far-field optical nanoscopy, Science **316**, 1153 (2007).

[19] J. Requejo-Isidro, Fluorescence nanoscopy. Methods and applications, J. Chem. Biol. **6**, 97 (2013).

[20] M. Sivaguru, M.A. Urban, G. Fried, C.J. Wesseln, L. Mander, and S.W. Punyasena, Comparative performance of airyscan and structured illumination superresolution microscopy in the study of the surface texture and 3D shape of pollen, Microsc. Res. Tech. **81**, 101 (2016).

[21] C.J.R. Sheppard, Super-resolution in confocal imaging, Opt. **80**, 53 (1988).

[22] C.J.R. Sheppard, S.B. Mehta, and R. Heintzmann, Superresolution by image scanning microscopy using pixel reassignment, Opt. Lett. **38**, 2889 (2013).

[23] S. Roth, C.J.R. Sheppard, K. Wicker, and R. Heintzmann, Optical photon reassignment microscopy (OPRA), Opt. Nanosc. **2**, 5 (2013).

[24] C.B. Müller and J. Enderlein, Image scanning microscopy, Phys. Rev. Lett. **104**, 198101 (2010).

[25] C. Roider, R. Heintzmann, R. Piestun, and A. Jesacher, Deconvolution approach for 3D scanning microscopy with helical phase engineering, Opt. Express **24**, 15456 (2016).

[26] M. Castello, G. Tortarolo, M. Buttafava, T. Deguchi, F. Villa, S. Koho, L. Pesce, M. Oneto, S. Pelicci, L. Lanzanó, et al., A robust and versatile platform for image scanning microscopy enabling super-resolution FLIM, Nat. Methods **16**, 175 (2019).

[27] J. Huff, The Airyscan detector from ZEISS: Confocal imaging with improved signal-to-noise ratio and super-resolution, Nat. Methods **12**, i (2015).

[28] G.M.R. De Luca, R.M.P. Breedijk, R.A.J. Brandt, A.H.C. Zeelenberg, B.E. de Jong, W. Timmermans, L.N. Azar, R.A. Hoebe, S. Stallinga, and E.M.M. Manders, Re-scan confocal microscopy: scanning twice for better resolution, Biomed. Opt. Express **4**, 2644 (2013).

[29] J. Schindelin, I. Arganda-Carreras, E. Frise, V. Kaynig, M. Longair, T. Pietzsch, S. Preibisch, C. Rueden, S. Saalfeld, B. Schmid, et al., Fiji: An open-source platform for biological-image analysis, Nat. Methods **9**, 676 (2012).

[30] F. de Chaumont, S. Dallongeville, N. Chenouard, N. Hervé, S. Pop, T. Provoost, V. Meas-Yedid, P. Pankajakshan, T. Lecomte, Y.L. Montagner, et al., Icy: An open bioimage informatics platform for extended reproducible research, Nat. Methods **9**, 690 (2012).

[31] D. Sage, L. Donati, F. Soulez, D. Fortun, G. Schmit, A. Seitz, R. Guiet, C. Vonesch, and M. Unser, DeconvolutionLab2: An open-source software for deconvolution microscopy, Methods **115**, 28 (2017).

[32] W.H. Richardson, Bayesian-based iterative method of image restoration, J. Opt. Soc. Am. **62**, 55 (1972).

[33] L.B. Lucy, An iterative technique for the rectification of observed distributions, Astron. J. **79**, 745 (1974).

[34] M. Minsky, Memoir on inventing the confocal scanning microscope, Scanning **10**, 128 (1988).

[35] C.J. Cogswell and K.G. Larkin, The specimen illumination path and its effect on image quality, in: *Handbook of Biological Confocal Microscopy*, 2nd ed., Ch. 8, ed. J.B. Pawley (Springer Science+Business Media, New York, 1995) pp. 127–137.

[36] W.V. Houston, A compound interferometer for fine structure work, Phys. Rev. **29**, 478 (1927).

[37] J.K. Fisher, A. Bourniquel, G. Witz, B. Weiner, M. Prentiss, and N. Kleckner, Four-dimensional imaging of *E. coli* nucleoid organization and dynamics in living cells, Cell **153**, 882 (2013).

[38] C.K. Spahn, M. Glaesmann, J.B. Grimm, A.X. Ayala, L.D. Lavis, and M. Heilemann, A toolbox for multiplexed super-resolution imaging of the *E. coli* nucleoid and membrane using novel PAINT labels, Sci. Rep. **8**, 14768 (2018).

[39] I. Schoen, J. Ries, E. Klotzsch, H. Ewers, and V. Vogel, Binding-activated localization microscopy of DNA structures, Nano Lett. **11**, 4008 (2011).

[40] A. Le Gall, D.I. Cattoni, B. Guilhas, C. Mathieu-Demazière, L. Oudjedi, J.-B. Fiche, J. Rech, S. Abrahamsson, H. Murray, J.-Y. Bouet, and M. Nollmann, Bacterial partition complexes segregate within the volume of the nucleoid, Nat. Communn. **7**, 12107 (2016).

[41] S. Wäldchen, J. Lehmann, T. Klein, S. van de Linde, and M. Sauer, Light-induced cell damage in live-cell super-resolution microscopy, Sci. Rep. **5**, 15348 (2015).

[42] J. Demmerle, C. Innocent, A.J. North, G. Ball, M. Müller, E. Miron, A. Matsuda, I.M. Dobbie, Y. Markaki, and L. Schermelleh, Strategic and practical guidelines for successful structured illumination microscopy, Nat. Protoc. **12**, 988 (2017).

[43] M. Iwai, M.S. Roth, and K.K. Niyogi, Subdiffraction-resolution live-cell imaging for visualizing thylakoid membranes, Plant J. **96**, 233 (2018).

[44] D. Aquino, A. Schönle, C. Geisler, C. v Middendorff, C.A. Wurm, Y. Okamura, T. Lang, S.W. Hell, and A. Egner, Two-color nanoscopy of three-dimensional volumes by 4Pi detection of stochastically switched fluorophores, Nat. Methods **8**, 353 (2011).

[45] S. Hell and E.H.K. Stelzer, Properties of a 4Pi confocal fluorescence microscope, J. Opt. Soc. Amer. A **9**, 2159 (1992).

[46] J. Bewersdorf, R. Schmidt, and S.W. Hell, Comparison of I5M and 4Pi-microscopy, J. Microsc. **222**, 105 (2006).

VAIZDŲ REKONSTRUKCIJA IŠ VIENO PIKSELIO: KONFOKALINIO VAIZDINIMO RIBA

S. Streckaitė [a, b], D. Frolov [a], J. Chmeliov [b, c], A. Gelžinis [b, c], C. Ilioaia [a], S. Rimsky [d], R. van Grondelle [e], L. Valkūnas [b], A. Gall [a], B. Robert [a]

[a] *Paryžiaus Saklė universitetas, Esonas, Prancūzija*

[b] *Fizinių ir technologijos mokslų centro Molekulinių darinių fizikos skyrius, Vilnius, Lietuva*

[c] *Vilniaus universiteto Fizikos fakulteto Cheminės fizikos institutas, Vilnius, Lietuva*

[d] *Paryžiaus mokslų ir literatūros tyrimų universitetas, Paryžius, Prancūzija*

[e] *Amsterdamo laisvojo universiteto Fizikos ir astronomijos fakultetas, Amsterdamas, Olandija*

Santrauka

Šviesos nanoskopija sulaukia didelio susidomėjimo vizualizuojant fluorescencines struktūras nanometrų skalėje. Pastaruoju metu difrakcijos ribą įveikė įvairūs nanoskopijos metodai, tačiau praktiškai juos dažnai riboja specialių fluoroforų poreikis, netrivialus gautų duomenų apdorojimas arba didelė kaina bei sudėtingas techninis įgyvendinimas. Dėl šių priežasčių konfokalinė mikroskopija, pasižyminti palyginti maža skiriamąja geba, vis dar yra dominuojantis metodas biomoksluose. Anksčiau buvo parodyta, kad vaizdo skenavimo mikroskopija (*Image Scanning Microscopy*; ISM) su matriciniu detektoriumi gali pagerinti konfokalinės mikroskopijos skiriamąją gebą. Šiame darbe apžvelgiame konfokalinės mikroskopijos principus ir pateikiame paprastą metodą, pagrįstą ISM, taikant kitokį vaizdo suformavimo būdą. Šį metodą galima lengvai įgyvendinti bet kurioje vaizdinimo sistemoje, pagrįstoje lazeriniu skenavimu su kameros detekcija, ir eksperimentiškai pasiekti teorinę konfokalinės mikroskopijos skiriamosios gebos ribą. Mūsų metodas, vieno pikselio rekonstrukcijos vaizdinimas (*Single Pixel Reconstruction Imaging, SPiRI*), leidžia atlikti didelės raiškos 3D vaizdinimą, naudojant vaizdų formavimą tik iš vieno kiekvieno įrašyto kadro pikselio. Mes pasiekiame eksperimentinę 330 nm *z* plokštumos skiriamąją gebą, kuri anksčiau nebuvo parodyta įprastose konfokalinėse ar ISM pagrįstose vaizdinimo sistemose. SPiRI metodas pasižymi mažu *xy* plokštumos ir *z* plokštumos skiriamųjų gebų FWHM santykiu, o tai reiškia didelį 3D fluorescencinio vaizdo pagerėjimą. Siekdami pademonstruoti SPiRI, pristatome didelio tikslumo 3D bakterijų chromosomos struktūrą.